Available online at www.sciencedirect.com
SCIENCE DIRECT
Coordination Chemistry Reviews 250 (2006) 1605–1620
COORDINATION CHEMISTRY REVIEWS
www.elsevier.com/locate/ccr

Review

Lanthanide "second-generation" precursors for MOCVD applications: Effects of the metal ionic radius and polyether length on coordination spheres and mass-transport properties

Graziella Malandrino, Ignazio L. Fragalà *

Dipartimento di Scienze Chimiche, Università di Catania, and INSTM, UdR Catania, Viale A. Doria 6, I-95125 Catania, Italy

Received 3 November 2005; accepted 13 March 2006
Available online 28 March 2006

Contents

Abstract

The panorama of trishexafluoroacetylacetonato polyether complexes of rare-earth metals is considered. The methods of preparation have been classified according to the nature of the starting rare-earth metal. The relationship between the coordination sphere and mass-transport properties is discussed as well as applications of these adducts to metal organic chemical vapor deposition (MOCVD) processes of rare-earth containing films. This review represents the first comprehensive study of the "second-generation" MOCVD rare-earth metal precursors from syntheses to applications.

Keywords: MOCVD; Rare-earth; Adducts; Volatility; Thermal stability; Thin films

1. Introduction

Chemical vapor deposition (CVD) processes have been of increasing commercial importance over the past decades [1]. Today metal organic CVD (MOCVD) [2] is becoming a preferred challenge among the CVD approaches since it by-passes undesired end-products often present in CVD processes in form of corrosive halogenydric acid etchers. In some cases, MOCVD almost represents a 'must', despite the more complex nature of the metal source, since it opens-up routes to a large variety of materials otherwise not-accessible [2–4]. This is the case of deposition of alkaline- and rare-earth containing films, since it is very difficult to find simpler CVD inorganic sources suitable for the deposition. The MOCVD technique uses volatile and thermally stable metallorganic precursor complexes and, in particular, metal β-diketonates have been widely used in the fabrication of metal oxide thin films [4–7]. Metal β-diketonates M(RCOCHCOR)$_x$ (where R = alkyl, aryl, etc.) are amongst the

* Corresponding author. Tel.: +39 095 7385055; fax: +39 095 580138.
E-mail address: lfragala@dipchi.unict.it (I.L. Fragalà).

0010-8545/$ – see front matter © 2006 Elsevier B.V. All rights reserved.
doi:10.1016/j.ccr.2006.03.017

most widely studied coordination compounds and have adequate characteristics in terms of mass-transport properties [8]. They were the first to be tested as MOCVD sources [7] and, therefore, they are usually referred as "first-generation" precursors. They, however, have shown several drawbacks in the case of large ionic radius metals due either to the formation of oligomeric species [9–13] or to coordination of water molecules [9,13,14].

With the perspective of a clear understanding of the specific requirements to be fulfilled in the design and the synthesis of rare-earth MOCVD precursors, we first discuss some of the basic principles of rare-earth element chemistry [15]. The rare-earth elements all show a stable 3+ oxidation state, which is the net charge that strikes the best balance between the ionization-energy cost and the lattice-energy or solvation-energy stabilization of the ion. Among the lanthanides, departure from the 3+ oxidation state occurs for those elements that can approach the $4f^0$, $4f^7$ or $4f^{14}$ configurations. In these cases 2+ or 4+ oxidation states can be stabilized. For example Ce, Pr and Nd (just past $4f^0$) and Tb and Dy (just past $4f^7$) show 4+ oxidation states; Sm and Eu (just short of $4f^7$) and Yb (just short of $4f^{14}$) show 2+ oxidation states. Note that, Ce is the only rare-earth element for which molecular precursors in the 4+ oxidation state are available [16,17], since for Pr, Nd, Tb and Dy the 4+ oxidation states are available only in the solid state.

For the lanthanides, the incomplete shielding of the nucleus by 4f electrons (relativistic effect) leads to a smooth contraction from $Z = 57$ to 71; thus a larger effective core charge contracts and stabilizes the 5p, 5d, 6s orbitals [18]. This trend is known as the *lanthanide contraction* and it has some chemical effects of interest [15]. The radii of the Ln^{3+} ions show a steady decrease from La^{3+} (1.17 Å) to Lu^{3+} (1.00 Å) [15]. Moreover, the radius of the main group Y^{3+} ion (1.04 Å) falls between those of Ho^{3+} and Er^{3+} and its chemistry closely resembles that of the late lanthanides [19]. The Ln^{3+} ions are large compared with most transition metal ions and this results in higher coordination numbers (usually greater than 6 and often as high as 9–10) in their complexes, compared with transition metal complexes where octahedral coordination is most commonly observed. The steady decrease of Ln^{3+} radius often results in structural changes as the series is traversed, with complexes of the early Ln^{3+} having greater coordination numbers than late elements.

In the wide scenario of emerging materials, rare-earth elements are components of several new interesting materials with properties ranging from high T_c superconductors, such as $LnBa_2Cu_3O_{7-\delta}$ [20,21], $Pb_2Sr_2LnCu_3O_{8-\delta}$ [22] and $La_{2-x}Sr_xCuO_4$ [23] to piezoelectrics such as $LaCuO_2$ [24] from buffer layers such as $LaAlO_3$ [25–27], $YAlO_3$ [28] and CeO_2 [16,29] to high k dielectrics such as Pr_2O_3 [30]. These materials all require suitable methodologies for their fabrication in the form of thin films that represent an unavoidable demand for their functional applications in emerging technologies.

In this context, the MOCVD technique offers a softer approach for all these applications, with lower processing temperatures and greater throwing power (versatility and adaptability) than alternative methodologies [1]. The conventional, "first-generation", rare-earth element precursors, such as $Ln(tmhd)_3$ (Htmhd = 2,2,6,6-tetramethyl-3,5-heptanedione) have shown several drawbacks, essentially associated with the significant residue left in commercial evaporators/bubblers and to poor stability to the atmosphere [31].

This behaviour may be due to the unsaturation of the inner coordination sphere that opens-up routes for easy polymerization or reaction either with donor solvents or nucleophilic impurities (such as water) that ultimately lead to low volatile polynuclear clusters or involatile oxo- or hydroxo-complexes [32].

All the limitations mentioned can be faced and overcome by modeling more complex molecular Ln architectures where hard polyether Lewis bases crowd and saturate the coordination sphere thus increasing the coordination number, competing with oligomerization and hydration side processes, and ultimately achieving steric saturation at the Ln center.

In this scenario, novel monomeric, thermally stable, volatile and water-free lanthanide complexes are of strategic relevance since they may fill the lack of MOCVD rare-earth precursors with suitable mass-transport properties. This consideration prompted investigations, in the 1990, on new suitable metal complexes with coordination spheres capable of: (i) inhibiting oligomerization and water coordination processes and (ii) improving the thermal stability, volatility and mass-transport properties. These studies go back over previous successful attempts, in which the combined use of fluorinated β-diketonates arrays and of ancillary coordinated polyethers were providing monomeric, volatile and thermally stable alkaline-earth metal sources, known as "second-generation" precursors [33–47]. Therefore, a similar strategy was applied to lanthanide ions yielding thermally stable, highly volatile and very promising "second-generation" lanthanide MOCVD precursors [48–68]. Most of them exhibit improved properties, in terms of thermal stability and volatility, thus being of potential interest for applications as precursors in the MOCVD of lanthanide containing phases [27,58,62,69,70]. They are also well suited as single precursors for the synthesis of fluoride and oxyfluoride phases, appealing materials as host matrices for luminescent ions [52,55,68,71]. As a matter of fact, fluorinated precursors may show some drawbacks due to the possible incorporation of undesired fluorine contaminants. Nevertheless, the excellent thermal stabilities and volatilities of this class of novel precursors as well as specific MOCVD protocols provide, for them, real improvements with respect to un-adducted β-diketonate "first-generation" MOCVD sources. On the other hand, to our knowledge, there are no fluorine free precursors with comparable mass-transport properties. In fact, the fluorine-free β-ketoiminate complexes, even though successfully applied to deposition of lanthanide oxides, are less volatile and less thermally stable than the fluorinated β-diketonate polyether adducts [72,73]. Other lanthanide complexes have been proposed as MOCVD or ALD precursors such as the La amidinates, but these compounds are also less volatile than the proposed adducts [74]. Finally, they may be applied as precursors in sol–gel technique processes since they are highly soluble in many organic solvents [75].

With this perspective, this contribution reports an overview of several prototypical rare-earth β-diketonate polyether

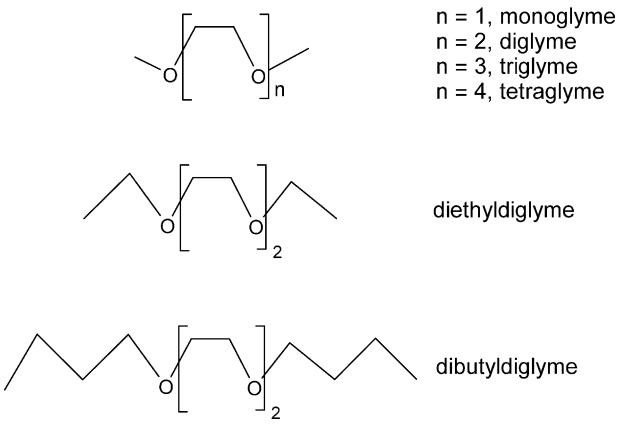

Chart 1.

adducts of general formula "Ln(hfa)$_3$·L" [Ln = La, Nd, Ce, Pr, Eu, Gd, Y; Hhfa = 1,1,1,5,5,5-hexafluoroacetylacetone, L = $CH_3O(CH_2CH_2O)_nCH_3$ with $n = 1$ *monoglyme* (dimethoxyethane), 2 *diglyme* (bis(2-methoxyethyl)ether), 3 *triglyme* (2,5,8,11-tetraoxadodecane) and 4 *tetraglyme* (2,5,8,11,14-pentaoxapentadecane), see Chart 1] from their syntheses to related MOCVD applications. The effect of the polyether length on the thermal stability, volatility and coordination sphere of the Ln(hfa)$_3$ moiety is discussed and the volatilities of the present adducts are compared to those of "first-generation" lanthanide precursors. In addition, the effects of the polyether lateral chains, such as in *diethyldiglyme* [bis(2-ethoxyethyl)ether] and in *dibutyldiglyme* [bis(2-butoxyethyl)ether], on the thermal properties of the adducts will be discussed for the Ce ion [62]. Accordingly, this review is divided into four main sections. Section 2 covers the methods of preparation, while Section 3 discusses the structural properties of the adducts and the variety of coordination modes of the polyether depending on the ionic radius of rare-earth metals. Section 4 correlates the coordination modes of the adducts with their thermal properties and transport characteristics. Applications of selected "Ln(hfa)$_3$·L" complexes as MOCVD precursors of rare-earth oxide based thin films are discussed in Section 5.

2. Synthesis of "Ln(hfa)$_3$·L" adducts

The "Ln(hfa)$_3$·L" adducts can be easily prepared through one-pot reactions by mixing in suitable solvents (benzene or dichloromethane) rare-earth oxides [Ln = La [51,55], Nd [64], Eu [53,63], Gd [52], Ho [60] Eq. (1)], hydroxides [Ln = Y [58], Eq. (2)] or nitrates (chlorides) [Ln = Ce [61,62], Pr [67,68], Eq. (3)] and hexafluoroacetylacetone and polyether ligands:

$$\begin{aligned}&La_2O_3 + 6Hhfa + 2L\\ &\rightarrow 2[La(hfa)_3\cdot L\cdot H_2O] + H_2O \text{ or } 2[La(hfa)_3\cdot L']\\ &+ 3H_2O \quad (L = \text{monoglyme; } L' = \text{diglyme,}\\ &\text{triglyme, tetraglyme}) \qquad (1)\end{aligned}$$

$$\begin{aligned}&2Y(OH)_3\cdot nH_2O + 6Hhfa + 2L\\ &\rightarrow 2[Y(hfa)_3\cdot L] + (n+6)H_2O \text{ or } 2[Y(hfa)_3\cdot(H_2O)_2]\cdot L'\\ &+ (n+2)H_2O \text{ or } [Y(hfa)_2\cdot L'']^+[Y(hfa)_4]^- + L''\\ &+ (n+6)H_2O \quad (L = \text{monoglyme, diglyme;}\\ &L' = \text{triglyme; } L'' = \text{tetraglyme}) \qquad (2)\end{aligned}$$

$$\begin{aligned}&Ce(NO_3)_3\cdot nH_2O + 3Hhfa + L + 3NaOH\\ &\rightarrow [Ce(hfa)_3\cdot L] + 3NaNO_3 + (n+3)H_2O\\ &(L = \text{diglyme, diethyldiglyme, dibutyldiglyme}) \qquad (3)\end{aligned}$$

A slight excess of the metal source favors the isolation of the complexes, but does not affect the purity of products since the insoluble excess of the metal reagent can be easily filtered off. The syntheses can be efficiently carried out in hexane or dichloromethane and produce with high yields non-hygroscopic and, in most cases, water-free adducts. The ancillary polyethers, therefore, act as hard Lewis bases that encapsulate the metal ion, favorably compete either with H_2O or with other weak ligands in saturating the coordination sphere around the metal and, finally, preclude any oligomerization.

In a few cases, one or two H_2O molecules coordinate to the metal center, due to the unfavorable balance between the ionic radius and the ligand branching. Thus, in the case of the monoglyme adduct of a large metal such as La, one H_2O molecule coordinates to the central ion and, hence, the monoglyme cannot efficiently act as a partitioning agent [55]. Any attempt to produce water-free monoglyme adducts, even using a 1:2 La:monoglyme excess ratio in the reaction mixture, proved unsuccessful. Oily products, whose nature prevented any further purification/crystallization, were always obtained.

At variance with the monoglyme La adduct, the homologous complexes of rare-earth ions with smaller ionic radii (e.g. Gd [52], Eu [53,63], Y [58]) are water-free. In these cases, the smaller radii enable the monoglyme to precisely encapsulate the metal ions, thus preventing any water coordination.

Interesting enough, some H_2O molecules coordinate to the small ionic radius metal center in the case of triglyme adducts. This apparently unexpected behaviour, found in the case of Y [57,58] and Ho [59], finds a clear rationale in the favorable matching between the too small ionic radii and the coordinatively redundant triglyme, too long to be coordinated as an inner sphere ligand. Thus, outer sphere complexes are obtained and the necessary coordination number is attained with two H_2O molecules.

All these adducts are very soluble in both polar and non-polar common organic solvents including ethanol, chloroform, acetone, pentane, toluene and slightly soluble in cyclohexane. They, in addition, have low-melting points and can be easily and quantitatively evaporated from the liquid phase at low temperature under vacuum. These are both key prerequisites for MOCVD applications (vide infra) and therefore, they may be used as liquid precursors for MOCVD processes.

3. Coordination spheres of rare-earth adducts

It is well known that the coordination sphere of any central metal ion crucially depends on the subtle interplay between the ionic radius and the ion charge. Namely, for a given charge, the larger the ion the higher is the coordination number. In the case of the alkaline earth metals, coordination numbers up to 11 have been observed in the case of the large Ba metal [44].

Lanthanides are similarly large in terms of ionic radii but, in contrast to the alkaline earth ions, they are 3+ ions. Thus, the "tris" Hhfa ligation already provides a six oxygen atoms environment. Nevertheless, six-coordination is usually not sufficient to complete the lanthanide coordination sphere and a neutral ligand of appropriate length is required to yield complexes with chemical–physical properties suitable for MOCVD applications. We have demonstrated that mass-transport properties are strictly correlated to coordination spheres and that a fine tailoring of properties of interest for MOCVD applications is possible by adjusting the architectural framework of the complexes.

3.1. Large rare-earth ions (La, Nd, Pr): the "La(hfa)$_3$·L" adducts

Lanthanum complexes represent a versatile example of large ionic radius rare-earth adducts. The ORTEP drawings of [La(hfa)$_3$·monoglyme·H_2O] (La-1), [La(hfa)$_3$·diglyme] (La-2), [La(hfa)$_3$·triglyme] (La-3) and [La(hfa)$_3$·tetraglyme] (La-4) are reported in Figs. 1–4, respectively. Fine details of the structures may be found in Refs. [51,55]. In general terms, the structures of La-1 and La-2 consist of asymmetric units containing, respectively, two and one molecule, consisting of a mononuclear nine-coordinate array with a square antiprismatic geometry. In the case of La-1 (Fig. 1) the oxygen ligation sites include the (hfa)$_3$ cluster (six oxygen atoms), the monoglyme ligand (two oxygen atoms) and one H_2O molecule capping one face. In the adduct La-2 (Fig. 2) in addition to the six-coordination of the hfa framework, the three oxygen atoms of the diglyme ligand are all involved in the coordination, with one of the oxygen atoms [O8] (Fig. 2) capping one of the square faces.

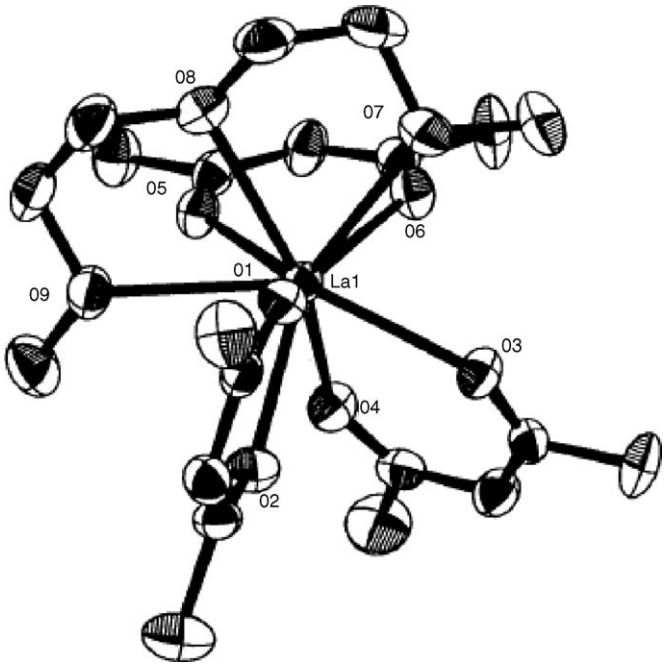

Fig. 2. ORTEP drawing of the crystal structure of La(hfa)$_3$·diglyme. CF_3 groups have been omitted for clarity [51,55].

It is interesting to contrast the average La-O(glyme) bond distances (2.613 Å in La-1 and 2.547 Å in La-2) with those found in the similarly nine-coordinate adduct [La(tmhd)$_3$·tetraglyme] (2.706–2.781 Å) [31]. The shorter contacts are indicative of stronger bonds between the La center and the polyether donor atoms. This observation finds counterpart in the fragmentation observed in mass spectra, where the $[Ln(hfa)_2{\cdot}L]^+$ usually represents the most intense (100%) peak and in the excellent thermal

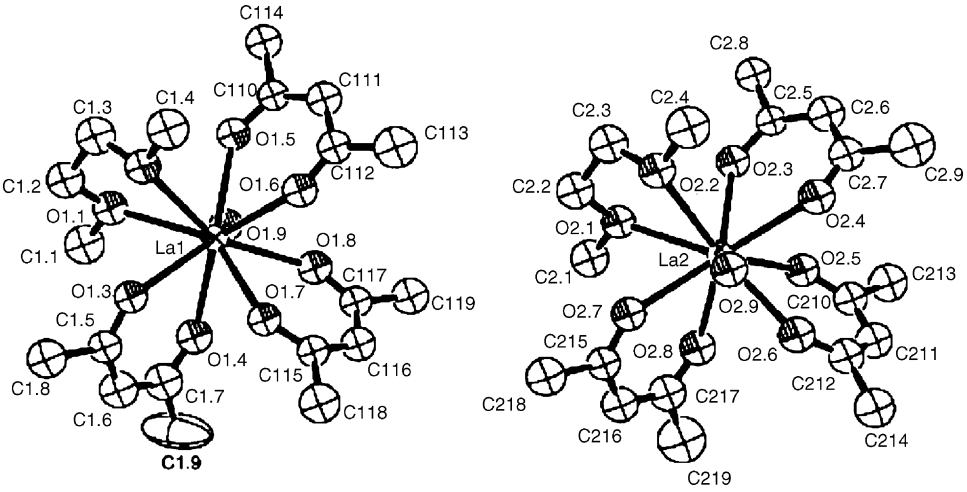

La(hfa)$_3$•monoglyme•H_2O

Fig. 1. ORTEP drawing of the asymmetric unit in the crystals of La(hfa)$_3$·monoglyme·H_2O. CF_3 groups have been omitted for clarity [55].

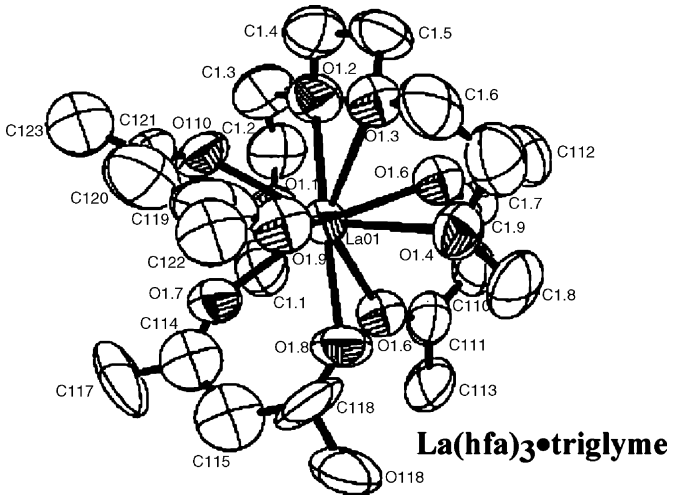

Fig. 3. ORTEP drawing of one of the four molecules present in the asymmetric unit of La(hfa)$_3$·triglyme. CF_3 groups have been omitted for clarity [55].

stabilities of these adducts. The crystal structure of La-3 consists of a very complex asymmetric unit with four rather similar molecules each containing a ten-coordinate lanthanum(III) ion (Fig. 3). There is no evidence of sizeable contacts within the four molecules of the asymmetric units. Such a crowded ten-coordination represents a real limit even for these large rare-earth cations. An expected consequence is, therefore, that in the case of the even longer tetraglyme only four among the five donor atoms are involved in the coordination. Thus, single crystal X-ray diffraction data of La-4 point to a mononuclear complex with a ten-coordinate lanthanum atom encapsulated by the six oxygen atoms of the (hfa)$_3$ cluster and four (among the potential five) O-donor atoms of the tetraglyme. The uncoordinated oxygen atom lies far from the metal ion (5.460 Å). The coordination polyhedron surrounding the La ion can be described as a distorted bicapped antiprism with O6 and O9 in the capping positions (Fig. 4).

3.2. Small rare-earth ions (Eu, Gd, Y): the "Y(hfa)$_3$·L" adducts

Smaller rare-earth ions, similarly react with hfa and various glymes through the same, viable one-pot synthetic procedures (vide supra). Remarkable changes of molecule architectures are, however, observed in related complexes of sterically less demanding later rare-earth ions. The following series involving the common "Y(hfa)$_3$" core and various glymes ancillary ligands represents a case study [57,58]. In fact, the [Y(hfa)$_3$·monoglyme] (Y-1) consists (Fig. 5) of an eight-coordinate polyhedron, involving all the six (hfa) and the two (monoglyme) oxygen donor atoms. The coordination remains lower than in the larger La cation, with a highly distorted polyhedral arrangement. In the Y complex, steric encumbrance prevents any H_2O ligation.

The greater nine-coordination, similar to that observed in larger cations, is found in the orthorhombic [Y(hfa)$_3$·diglyme] (Y-2) (Fig. 6) [58]. In this case, the coordination sphere includes the six "hfa" oxygen atoms and all the three oxygen atoms of the diglyme ligand. Therefore, the stronger chelating capability of the ether oxygen forces, despite the smaller ionic radius, the formation of nine-coordination. A less symmetric monoclinic polymorph has also been reported for crystals of the same complex [57]. The next "Y(hfa)$_3$·triglyme" suffers a poor

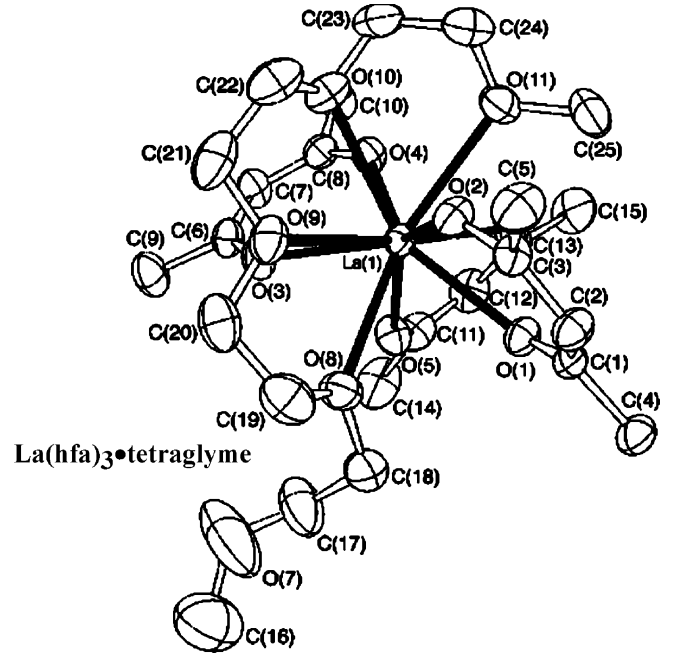

Fig. 4. ORTEP drawing of the crystal structure of La(hfa)$_3$·tetraglyme. CF_3 groups have been omitted for clarity [56].

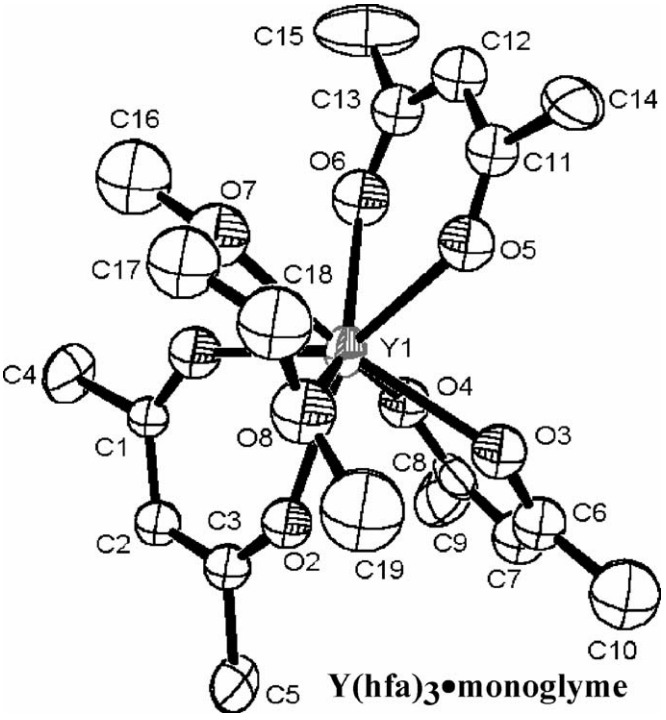

Fig. 5. ORTEP drawing of the crystal structure of Y(hfa)$_3$·monoglyme. CF_3 groups have been omitted for clarity [58].

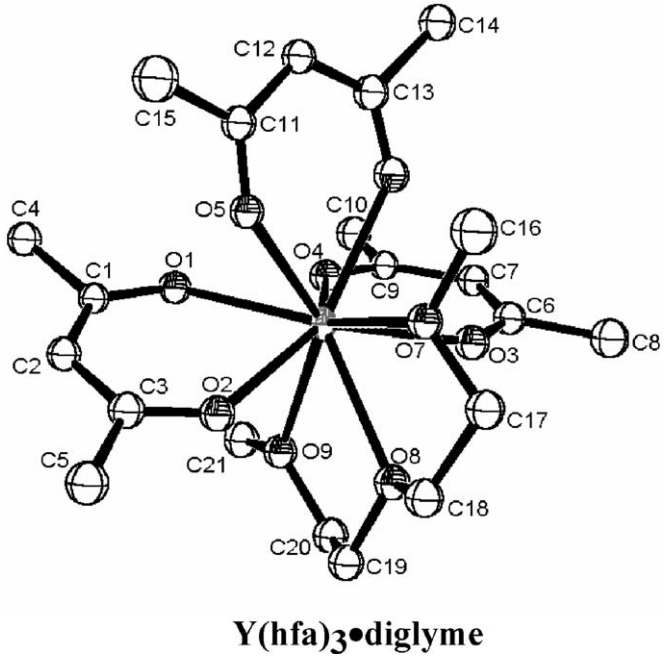

Fig. 6. ORTEP drawing of the crystal structure of $Y(hfa)_3$·diglyme. CF_3 groups have been omitted for clarity [58].

match between the triglyme, with four oxygen chelators, and the small metal ion. Therefore, X-ray single crystal data suggest an outer-sphere complex $[Y(hfa)_3\cdot(H_2O)_2]$·triglyme (Y-3) (Fig. 7) [57]. The ^1H NMR experiments similarly point to a 3:2:1 (hfa:H_2O:triglyme) ratio, and also the finger print region of the IR-spectrum indicates a different coordination.

Note that this complex is immediately formed adopting the one-pot route described, while it was obtained by sublimation from the ionic structure $[Y(hfa)_2\cdot\text{triglyme}]^+[Y(hfa)_4]^-$ by Pollard et al. [57].

Upon further increasing the polyether length, a suitable compromise between coordination requirements and the ion dimension can be obtained through the formation of ionic structures. In fact, the species involving the tetraglyme ligand consist of an ionic structure of the type $[Y(hfa)_2\cdot\text{tetraglyme}]^+[Y(hfa)_4]^-$ (Y-4) (Fig. 8) where the most suitable eight- or nine-coordination of the Y^{3+} ion is obtained [57]. It is, therefore, evident that longer glymes (tri- and tetra-) appear poorly suited for smaller ions and, as a consequence, form complexes that are less volatile and poorly thermally stable than encountered with larger metal ions.

In some cases, neutral structures with longer polyethers such as triglyme or tetraglyme linking two $Ln(tmhd)_2$ moieties (Ln = Y [48], Er [76], Eu [31], Tb [31], Gd [50]) have been observed. In these cases, both metal centers are eight-coordinate with the overall coordination polyhedron being distorted square antiprismatic.

Structural analogies between the present yttrium adducts and those of the lanthanide homologues deserve further comments. This series of complexes is analogous to those observed for Eu [53], Gd [52], and Ho [59,60,65] but is different from those observed for La [51,55] and Nd ions. In fact, in the

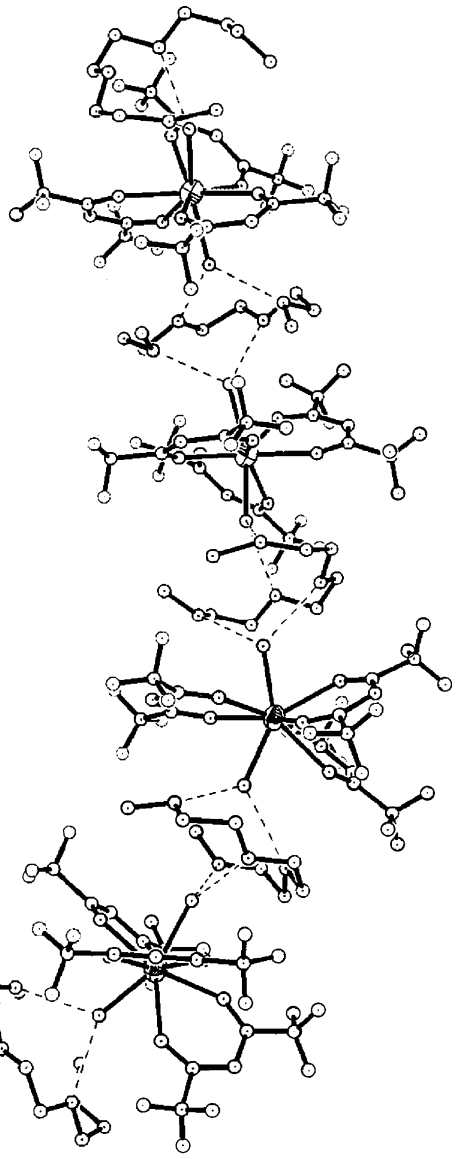

Fig. 7. ORTEP drawing of crystal structure of $Y(hfa)_3\cdot(H_2O)_2$·triglyme. Figure was reproduced from Ref. [57], with permission of the copyright holders.

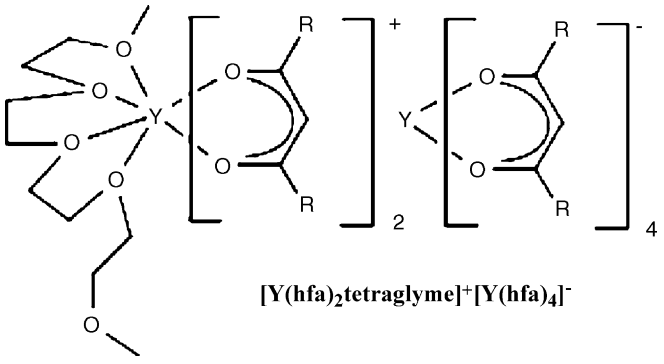

Fig. 8. Scheme of the $[Y(hfa)_2\cdot\text{tetraglyme}]^+[Y(hfa)_4]^-$ ionic structure.

Table 1
Crystal structure data of "Ln(hfa)$_3$·glyme" adducts[a]

Compound	Space group	Average M–O(β-diket) (Å)	Average M–O(L) (Å)	Ionic radius [15]	Coord. number	References
[La(hfa)$_3$·monoglyme·H$_2$O]	$P2_1/c$	2.512	2.616	1.17	9	[55]
[La(hfa)$_3$·diglyme]	$P2_1/c$	2.496	2.639	1.17	9	[51,55]
[La(hfa)$_3$·triglyme]	$P2_1/n$	2.509	2.675	1.17	10	[55]
[La(hfa)$_3$·tetraglyme]	$P2_1/n$	2.534	2.717	1.17	10	[56]
[La(tmhd)$_3$·tetraglyme]	$P2_1/n$	2.463	2.746	1.17	9	[31]
[Ce(hfa)$_3$·diglyme]	$P2_1/c$	2.475	2.626	1.15	9	[62]
[Pr(hfa)$_3$·diglyme]	$P2_1/c$	2.467	2.613	1.13	9	[68]
[Eu(hfa)$_3$·diglyme]	$P2_1/n$	2.403	2.553	1.09	9	[53]
[Gd(hfa)$_3$·diglyme]	$P2_1/n$	2.394	2.544	1.08	9	[52]
[Ho(hfa)$_3$·monoglyme]	$Pbca$	2.309	2.435	1.04	8	[60]
[Ho(hfa)$_3$·(H$_2$O)$_2$]·triglyme	$P2_1/c$	2.336	–	1.04	8	[59]
[Ho(hfa)$_2$·triglyme]$^+$[Y(hfa)$_4$]$^-$	$Fdd2$	2.310, 2.335	2.355	1.04	8	[65]
[Y(hfa)$_3$·monoglyme]	$Pcab$	2.342	2.466	1.04	8	[58]
[Y(hfa)$_3$·diglyme]	$Pc2_1n$	2.361	2.495	1.04	9	[58]
[Y(hfa)$_3$·(H$_2$O)$_2$]·triglyme	$P3(1)21$	2.340	–	1.04	8	[57]
[Y(hfa)$_2$·triglyme]$^+$[Y(hfa)$_4$]$^-$	$Fdd2$	2.298, 2.335	2.359		8	[57]

[a] The La(tmhd)$_3$·tetraglyme adduct has been included for comparison.

case of La, completely different coordination spheres have been found for the monoglyme, triglyme and tetraglyme adducts. This indicates that in these compounds the Y^{3+} behaves like a smaller lanthanide element. In fact, the average Y–O distances are similar to those reported for the Gd and Ho adducts. In particular, the large difference (0.150 Å) observed between the average Y–O(diglyme) and the average Y–O(hfa) distances (Table 1) in the Y(hfa)$_3$·diglyme are exactly the same of that observed in the Gd derivative and much larger than that reported (0.014 Å) for the La analogue. These data may be interpreted by considering the ionic radius values of La^{3+} (1.17 Å), Gd^{3+} (1.08 Å), Y^{3+} (1.04 Å), and Ho^{3+} (1.04 Å) ions. The metal–oxygen bond distances of various rare-earth adducts of the type "Ln(hfa)$_3$·diglyme" are reported in Table 1. Both the M–O(hfa) and the M–O(glyme) distances decrease upon contraction of the metal ion.

4. Mass-transport properties

Thermogravimetric and chemical vapor deposition experiments provide evidence of the "thermal robustness" and mass-transport properties of the adducts discussed. High vapor pressure values and very good thermal stabilities with a residue left lower than 4% have been generally found for almost all the precursors. Isothermal thermogravimetric (ITG) investigations have, when necessary, allowed very useful evaluation of both transport properties and of apparent vaporization enthalpies. Finally, interesting insights on other relevant properties have been obtained from differential scanning calorimetry (DSC) measurements.

The most relevant properties of the current molecular sources are collected in Table 2. Species that will be addressed in detail in the following section are italicized in the table.

Table 2
Physical data for "Ln(hfa)$_3$·glyme" adducts

Sample	Melting point[a] (°C)	Sublimation temperature (10^{-3} mmHg)	DSC data[b]	Thermal data	Reference
[La(hfa)$_3$·monoglyme·H$_2$O]	60–64	75–80	47.1 (w.l.), 67.1 (m.), 220 (vap.)	Sublime intact	[55]
[La(hfa)$_3$·diglyme]	74–76	65–70	74.9 (m.), 240 (vap.)	Sublime intact	[51,55]
[La(hfa)$_3$·triglyme]	88–90	95–105	79.3 (p.t.), 87.6 (p.t.), 145.8 (m.), 230 (vap.)	Sublime intact	[51]
[La(hfa)$_3$·tetraglyme]	81–84	–	67 (p.t.), 84 (m.), 280 (vap.)	Multi step subl.	[56]
[Ce(hfa)$_3$·diglyme]	75–77	85–90	74.7 (m.), 245 (vap.)	Sublime intact	[62]
[Ce(hfa)$_3$·diethyldiglyme]	106–108	100–110	63.9 (p.t.), 107.9 (m.), 225 (vap.)	Sublime intact	[62]
[Ce(hfa)$_3$·dibutyldiglyme]	44–45	80–90	44.8 (m.), 255(vap.)	Sublime intact	[62]
[Pr(hfa)$_3$·diglyme]	69–73	75–80	–	Sublime intact	[68]
[Eu(hfa)$_3$·monoglyme]	80–82	75–80	81.2 (m.), 210 (vap.)	Sublime intact	[63]
[Eu(hfa)$_3$·diglyme]	72–74	85–90	71.4 (p.t.), 122.0 (m.), 220 (vap.)	Sublime intact	[63]
[Gd(hfa)$_3$·monoglyme]	80–81	75–80	80.7 (m.), 220 (vap.)	Sublime intact	[52]
[Gd(hfa)$_3$·diglyme]	71–74	75–85	69.8 (p.t.), 123.3 (m.), 220 (vap.)	Sublime intact	[52]
[Y(hfa)$_3$·monoglyme]	74–77	75–80	75.7(m.), 175 (vap.)	Sublime intact	[58]
[Y(hfa)$_3$·diglyme]	60–63	80–85	62.2 (m.), 210 (vap.), 220 (ex.)	Sublime intact	[58]
Y(hfa)$_3$·(H$_2$O)$_2$·triglyme	52–55	95–100	53.8 (m.), 235 (ex.), 250 (vap.)	Multi step subl.	[58]
[Y(hfa)$_2$·tetraglyme]$^+$[Y(hfa)$_4$]$^-$	175–178	130–140	176.9 (m.), 248.6 (ex.), 275 (vap.)	Sublime intact	[58]

[a] Melting points have been observed with a Koffler microscope.
[b] w.l., water loss; m., melting; p.t., transition to plastic phase; ex., exothermic peak; vap., vaporization.

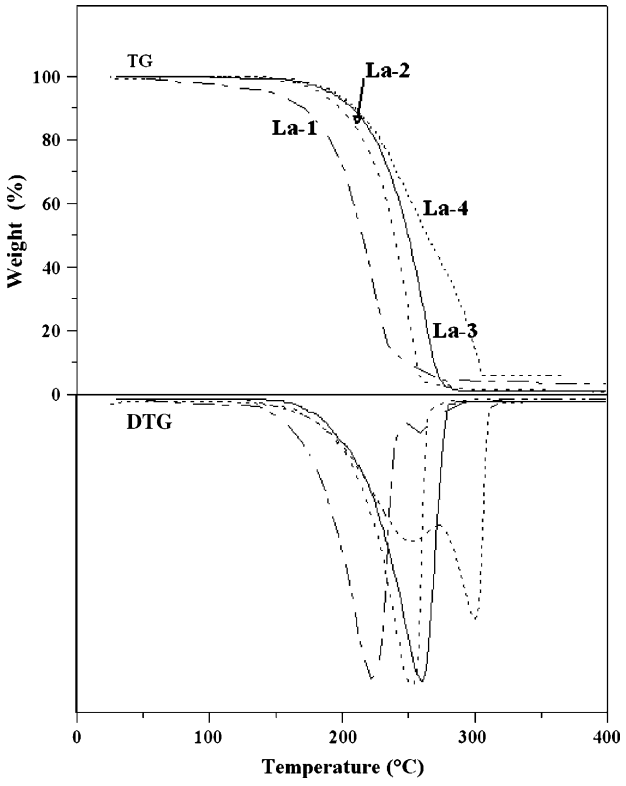

Fig. 9. TG–DTG curves of the "La(hfa)$_3$·glyme" adducts.

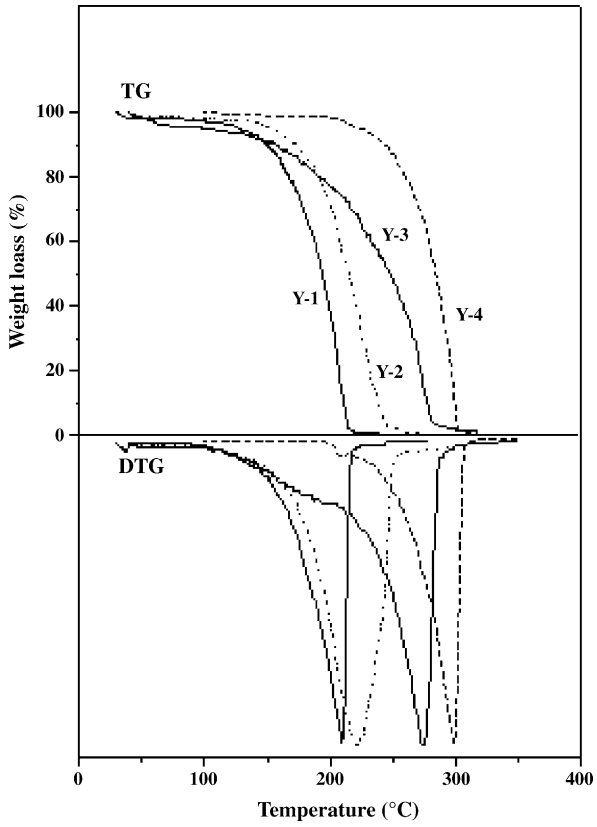

Fig. 10. TG–DTG curves of "Y(hfa)$_3$·glyme" adducts.

4.1. Thermogravimetric and vaporization rate of "Ln(hfa)$_3$·L"

Mass-transport properties of these metal precursors represent key aspects for their functional validation. With this perspective, atmospheric and low pressure thermal gravimetric analyses (TG) and differential thermal gravimetric (DTG) and isothermal gravimetric experiments provide useful information. The TG curves of some "La(hfa)$_3$·L" are reported in Fig. 9. The La-1 adduct shows a 89% weight loss in the 53–251 °C range and a 7% loss in the 251–341 °C range with a 4% total residue left at 350 °C. Singular sublimation steps are observed for the La-2 and La-3 adducts in the temperature ranges of 115–295 °C (residue = 2% to 300 °C) and 143–296 °C (residue = 1% to 300 °C), respectively. La-4 shows two vaporization steps in the 150–300 and 300–340 °C ranges with a 5% residue left at 355 °C. Therefore, it is less stable than the other related complexes. TGA atmospheric pressure vaporization rates of adducts La-1, La-2, La-3 and La-4 indicate they vaporize ca. 29×, 12×, 7× and 3× more rapidly than La(tmhd)$_3$·H$_2$O, respectively.

Fig. 10 displays TG data for the yttrium parent adducts. Single sublimation steps are observed for the Y-1, Y-2 and Y-4 adducts. Y-1 adduct shows a 96% weight loss in the 79–220 °C range with a 4% residue left at 275 °C. Vaporization processes of Y-2 and Y-4 occur in a higher temperature range, namely 90–260 °C (residue = 2% to 300 °C) and 170–330 °C (residue = 4% to 400 °C) in the two cases, respectively. By contrast, Y-3 undergoes two distinct processes in the 80–300 °C with a residue left of ≈11%. Namely, a 29% loss is observed in the 80–230 °C temperature range and 60% in the 230–300 °C temperature range. The process related to the first step is likely due to loss of the triglyme and of the coordinated H$_2$O, weakly bonded ligands (expected weight loss ≈22%). In the higher 220–300 °C range, vaporization of the naked Y(hfa)$_3$ causes the loss of an additional 60%. This behaviour, clearly dependent on the weakly coordinated H$_2$O and triglyme ligands, is closely reminiscent of that observed in the case of other hydrated β-diketonates as [Y(tmhd)$_3$·H$_2$O]$_2$ [77,78]. Therefore, H$_2$O is not an "innocent" or "spectator" ligand, but it plays a key role in the chemistry of mentioned precursors.

In regard to vaporization rates of Y-1, Y-2, Y-3 and Y-4 in comparison to data of [Y(tmhd)$_3$·H$_2$O]$_2$, it becomes evident that Y-1 and Y-2 adducts are more volatile than the "first-generation" [Y(tmhd)$_3$·H$_2$O]$_2$ precursor, and in particular, vaporize ca. 4× and 2× more rapidly, respectively. Adduct Y-3 shows a non-linear behaviour of the vaporization rate as expected for a process accompanied by some partial decomposition. Finally, a low vaporization rate is observed for Y-4. This is not unexpected due to its ion-pair [Y(hfa)$_2$·tetraglyme]$^+$[Y(hfa)$_4$]$^-$ nature.

4.2. Differential scanning calorimetry analyses "Ln(hfa)$_3$·L"

Differential scanning calorimetric data provide insights on processes involving present sources depending upon the temperature. The DSC curves show some interesting features, in addition to expected evidences of melting and evaporation. In

particular, the La-1 adduct shows three endothermic peaks at 47.9, 62.5 and 111.8 °C. The first two peaks may be associated with solid state polymorphic transitions, while the third represents the melting process. The compound vaporizes in the 160–240 °C temperature range. The DSC curves of La-2 precursor show endothermic peaks due to melting at 74.9 °C and evaporation at 250–280 °C. The La(hfa)$_3$·triglyme shows some interesting features in terms of four endothermic peaks. The first two peaks at 79.3 and 87.6 °C are thermal anomalies likely associated with transitions to plastic phases. The third peak is associated with the adduct melting while the fourth broad peak represents the evaporation process.

The curve of the La-4 adduct shows the presence of two sharp peaks at 67 and 84 °C, indicating that the adduct undergoes a reversible phase transition at the lower temperature and completely melts at 84 °C. Evaporation occurs in the 280–320 °C temperature range.

The DSC curve of the Y-1 adduct shows two endothermic peaks at 75.7 °C associated with melting of the product and at ∼175 °C due to evaporation. The DSC curve of adduct Y-2 similarly shows two endothermic peaks associated with melting (62.2 °C) and evaporation processes (∼150 °C), respectively. Moreover, there is evidence at 220 °C of an exothermic peak that is observed both in the freshly prepared as well as in aged (over 4 months) samples.

The adduct Y-3 shows a broad endothermic peak at 53.8 °C which can be mainly associated with the melting of the product. Nevertheless, it is likely that some other kind of processes, i.e. a solid phase transition peak, may be hidden under the same peak. A second endothermic peak (∼250 °C) is associated with the evaporation of the adduct. Similar to adduct Y-2, an exothermic peak is observed at 235 °C.

The adduct Y-4 shows two endothermic peaks at 176.9 °C, associated with the melting process and at ∼275 °C due to evaporation. An exothermic peak has been also found at 248.6 °C. In Fig. 11 some peculiar DSC curves are reported.

It is very interesting to observe the melting point variation for the various adducts as a function of the ionic radius and coordination sphere (Table 2). There is evidence that for similar coordination environments the melting points are almost independent of the nature of the central metal ion. By contrast, in the case of the tetraglyme adducts of La and Y completely different melting points are observed since the different ionic radii favor remarkable differences of related crystal structures.

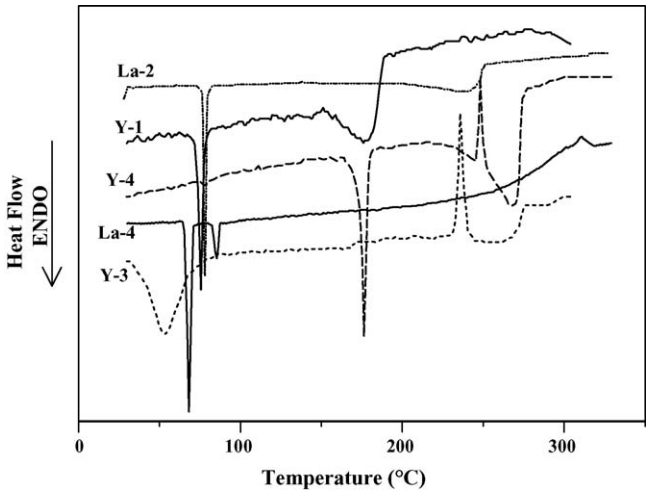

Fig. 11. DSC curves of "Ln(hfa)$_3$·glyme" adducts.

4.3. Relationship between the coordination sphere of "Ln(hfa)$_3$·L" adducts and thermal properties

It has been already stressed that, to our knowledge, the present "second-generation" rare-earth precursors represent the first examples, among β-diketonate species, of thermally stable and highly volatile precursors which vaporize intact even under atmospheric pressure. These properties, appealing for MOCVD applications, are crucially driven by the fluorinated framework. Fluorine, in fact, acts both on volatility and thermal stability. Thus, fluorinated β-diketonates are much more volatile than the parent fluorine free complexes. This is due to two different factors: the presence of fluorine precludes the formation of intermolecular H bonds and, moreover, favors the formation of less packed structures in the lattice due to the bulkier, relative to H, dimensions [8]. Beside these effects that favor less congested lattice structures, the electron withdrawing effect of the fluorine atoms renders the β-diketonate ligands much more acidic than the analogous fluorine-free ligands. This increases the net positive charge on the metal ion and, as a consequence, causes electron deficiency at the metal center that favors hard–hard interactions with Lewis base ligands. By contrast, coordination of the glyme ancillary ligands to fluorine free β-diketonate complexes, as in the case of the analogous La(tmhd)$_3$·tetraglyme, results in species that undergo easy decomposition upon sublimation in vacuo, thus yielding the un-adducted tmhd complexes [31].

Polyether ancillary ligands play a crucial role as well and related evidence can be well addressed upon consideration of properties of the La and Y adducts, that are the two case studies of the present review. Thus, in the case of the lanthanum adducts there is evidence that a lengthening of the polyether chain parallels a decrease in volatility. In fact, the short bischelator, monoglyme, forms a very volatile lanthanum precursor La-1 (Table 1, Fig. 1), which unfortunately has an additional H_2O coordinated molecule. The longer diglyme and triglyme polyethers fit well the metal ion requirements and form the adducts La-2 and La-3 with good properties in terms of thermal stability and volatility. Finally, the longer tetraglyme exceeds, with the five oxygen donor atoms, the acceptor capabilities of the La(III) ion and, as a consequence, one oxygen atom is left as a spectator [56]. This adduct (La-4) has poorer volatility among the four lanthanum adducts and, similarly poorer stability with respect to the adducts obtained with the shorter glymes.

In the case of the Y^{3+} family, the polyether length also plays a crucial role since it affects the coordination sphere around the yttrium ion and, hence, the thermal properties and volatilities of related adducts. There is, in fact, evidence of an intriguing interplay between the polyether chain length and the yttrium ionic radius in determining the volatility of these adducts. Therefore, small polyethers, such as the monoglyme or diglyme, form

the more volatile precursors Y-1 and Y-2. The longer triglyme and tetraglyme parent adducts have more complex coordination spheres and form the less volatile and relatively poor thermally stable adducts Y-3 and Y-4. In fact, the coordinated H_2O molecules in Y-3 are responsible for the two-step decomposition evaporation, while the proposed ionic structure of Y-4 finds a counterpart in the higher melting point and the consequent low volatility.

There is, therefore, evidence of an intriguing interplay between the polyether chain length and the rare-earth ionic radius in determining the volatility of these adducts, and only when the optimal coordination environment is reached will the complex show the best characteristic properties in terms of mass-transport properties. In particular, the best behaviour is observed for the optimal coordination number of 9 for La and of 8 for Y.

Finally, a short comment must be devoted to effects of branching alkyl arms present in the polyether chains. There is evidence that the branching arms have little effect, if any, on thermal properties once similar coordination environments are maintained relative to unsubstituted polyethers. Thus, the volatility and stability of [Ce(hfa)$_3$·glyme] [glymes = diglyme, diethyldiglyme and dibutyldiglyme] adducts [62] with branched diethyl- and dibutyldiglyme are almost comparable to those of the relative adduct with the simpler diglyme as observed in TG data. In all cases, in fact, similar coordination is observed around the Ce^{3+} ion. Nevertheless, the length of substituents appended to the polyether chain proved a suitable tool to finely tailor melting temperatures without significantly affecting volatilities. This is an important issue since low-melting precursors are highly desirable.

4.4. Solvent behaviour of "Ln(hfa)$_3$·glyme adducts: multi-element liquid single sources

The synthesis of any multi-element oxide film always introduces complications in the MOCVD growth process due to different physico-chemical properties of each single precursor that, of course, requires specific procedural optimizations. In recent years, we have proposed new, very simple, low-cost routes to high quality mixed oxides thin films adopting a multi-metal molten single source [27,58,70,79,80]. In the prototypical case of $LaAlO_3$ deposition on $SrTiO_3$ (1 0 0) substrates the novelty of the approach relies upon the use of the lower melting source, [La(hfa)$_3$·diglyme] as a solvent for the aluminum (or for all the remainders) precursor Al(acac)$_3$ (Hacac = acetylacetone), thus affording a two-component molten single source [27,79].

A particularly intriguing property of these low-melting [Ln(hfa)$_3$·L] adducts has been found associated with their capability to act as a solvent for other "first- or second-generation" precursors. These multi-metal liquid mixtures represent "single" sources that can be easily and cleanly evaporated from melt with constant mass-transport rates within constant stoichiometric ratios. By contrast, the adoption of singular metal solid sources requires separate controls for their sublimation processes from solids. In addition, there are additional and severe drawbacks associated with sintering and surface passivation of solids which render transport processes largely irreproducible [81]. Even more important, the use of the multi-metal single precursors implies simpler reactor design and easy control of deposition parameters, since individual sublimation–evaporation parameters and carrier gas flows are no longer required.

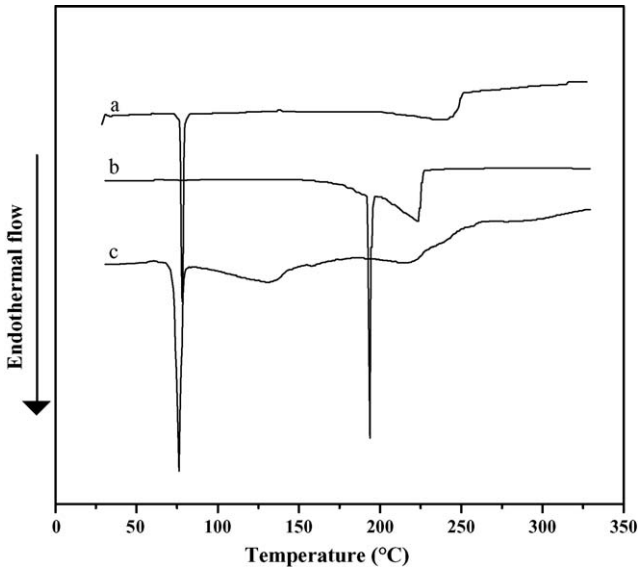

Fig. 12. DSC curve of the La(hfa)$_3$·diglyme and Al(acac)$_3$ 1:1 mixture (c) compared to the curves of the pure La(hfa)$_3$·diglyme (a) and Al(acac)$_3$ (b) precursors.

Two case studies of multicomponent mixtures have become paradigms and, in this context, the fabrication of thin films of $LaAlO_3$ [27,79] and $YBa_2Cu_3O_{7-\delta}$ [58] on $SrTiO_3$ (1 0 0) substrates will be addressed in detail. The La–Al multicomponent source consists of an homogeneous mixture of [La(hfa)$_3$·diglyme], and Al(acac)$_3$ in a 1:1 stoichiometric ratio. This source mixture has proven well suited to sustain constant mass-transport rates (also under atmospheric pressure) from the liquid phase. It is of interest to compare DSC data of the multi-metal La/Al source with those of the individual precursors (Fig. 12). Individual La and Al precursors show endothermic peaks due to melting (74.9 °C for [La(hfa)$_3$·diglyme] and 198.6 °C for Al(acac)$_3$) and to evaporation from melts (250–280 and 260–290 °C, respectively). The curve of the La/Al source shows a lower temperature peak (72.8 °C)[1] associated with melting of the [La(hfa)$_3$·diglyme] component and a broad endothermic peak (in the 85–160 °C temperature range) associated with Al(acac)$_3$ dissolution [27,79]. Interesting enough, the endothermic peak (198.6 °C) expected for the Al(acac)$_3$ melting is not observed. Optical microscope, polarised light and low pressure sublimation data of the two component mixture are in agreement with these conclusions. Isothermal gravimetric (ITG) analyses provide (Fig. 13) further insight on the thermal robustness and on mass-transport properties of the same multi-element source under experimental conditions similar to those used in MOCVD experiments. The mass loss depends linearly on the vaporization time in the 100–140 °C temperature range, under nitrogen flow at P_{tot} = 20 Torr. The linear trend indicates that the vaporization

[1] The lower temperature, compared to the pure compound, represents a cryoscopic effect.

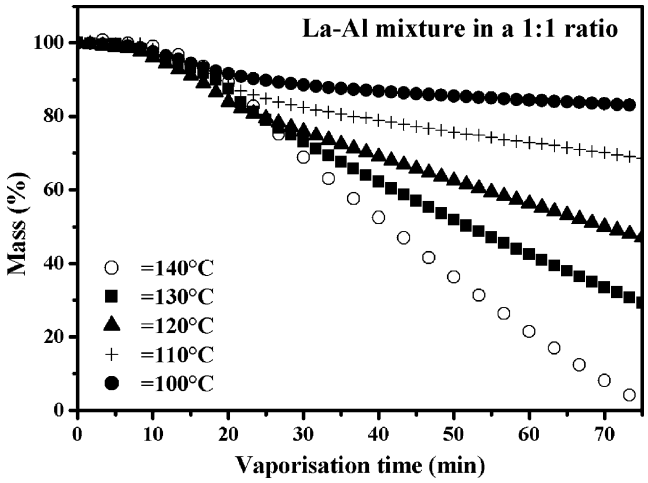

Fig. 13. Time dependence of weight loss during vaporization of $La(hfa)_3$·diglyme and $Al(acac)_3$ 1:1 mixture at various temperatures.

rate remains constant during the vaporization time for each temperature and that no side phenomena, such as decomposition or polymerization, affect the process.

The Arrhenius plots related to sublimation/evaporation processes of [$La(hfa)_3$·diglyme] and $Al(acac)_3$ precursors and of their 1:1 mixture point to clean processes involving similarly thermally stable sources (Fig. 14). The slopes of the plots provide the apparent sublimation/evaporation enthalpies associated with the different processes. Thus, the remarkably greater value found for the $Al(acac)_3$ (103 ± 7 kJ mol^{-1}) than for the [$La(hfa)_3$·diglyme] (66 ± 3 kJ mol^{-1}) and for the 1:1 mixture (56 ± 5 kJ mol^{-1}) is clearly due to the $Al(acac)_3$ sublimation from the solid phase, which requires more energy than evaporation occurring from the molten [$La(hfa)_3$·diglyme] adduct or from the 1:1 mixture.

There is no evidence of ligand exchange both in the gas phase and in the melted multicomponent mixture. In fact, the FAB mass spectrum of the 1:1 mixture shows only the peaks due to the fragmentation of individual precursors, namely [$La(hfa)_2$·diglyme]$^+$, [La(hfa)·diglyme + F]$^+$,

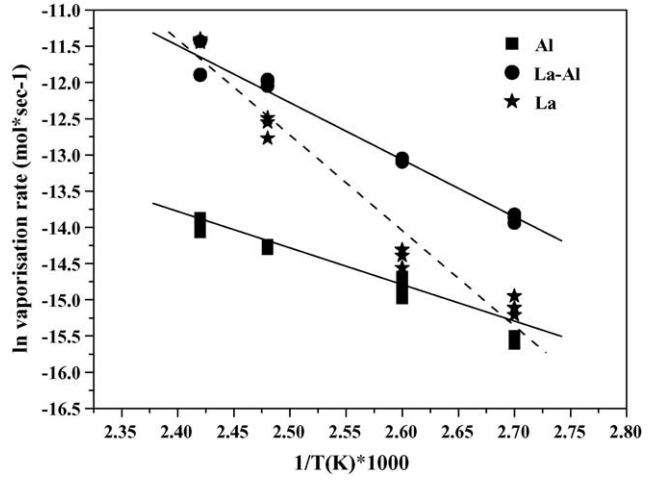

Fig. 14. Arrhenius plots for vaporization processes of: $La(hfa)_3$·diglyme and $Al(acac)_3$ 1:1 mixture, $La(hfa)_3$·diglyme, and $Al(acac)_3$.

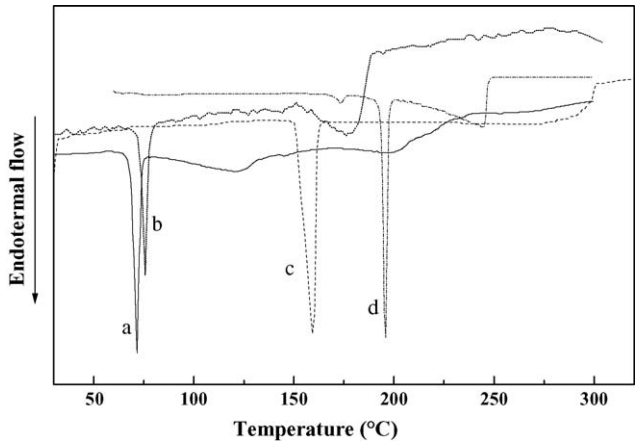

Fig. 15. DSC curve of the 1:2:0.5 (Y:Ba:Cu) multi-metal single source mixture (a) compared with data of individual precursors $Y(hfa)_3$·monoglyme (b), $Ba(hfa)_2$·tetraglyme (c), and $Cu(tmhd)_2$ (d).

[La·diglyme + 2F]$^+$ and [$Al(acac)_2$]$^+$. Moreover, preliminary ^{13}C MAS NMR experiments on the 1:1 melt (125 °C) show well-resolved resonances attributed to the individual precursors.

Similar behaviour was found with a more complex source system involving three components: [$Y(hfa)_3$·monoglyme], [$Ba(hfa)_2$·tetraglyme] and [$Cu(tmhd)_2$]. Also in this case the lower melting [$Y(hfa)_3$·monoglyme] becomes the solvent for the remaining precursors [58]. Thus, the endothermic melting peaks of [$Y(hfa)_3$·monoglyme] (75.7 °C), of [$Ba(hfa)_2$·tetraglyme] (153.6 °C) and of $Cu(tmhd)_2$ (196.3 °C) and those due to evaporation from melts (150–190, 260–290, and 210–260 °C temperature ranges, respectively) are evident in the DSC curves (Fig. 15). In the multi-metal (Y–Ba–Cu) source, the [$Y(hfa)_3$·monoglyme] represents the lower melting (73.5 °C) component that in the 110–160 °C range dissolves both [$Ba(hfa)_2$·tetraglyme] and $Cu(tmhd)_2$. The highest temperature (190–270 °C) endothermic process is, finally, associated with evaporation of the melted mixture. Similar to the previous case the endothermic peaks expected for the [$Ba(hfa)_2$·tetraglyme] and $Cu(tmhd)_2$ melting, at 153.6 and 196.3 °C, respectively, are no longer observed.

Similar behaviour was observed for other multicomponent mixtures, such as [$Ca(hfa)_2$·tetraglyme], [$Ba(hfa)_2$·tetraglyme] and $Cu(tmhd)_2$ used for the deposition of BaCaCuO(F) layers, precursor matrices of the $Tl_2Ba_2CaCu_2O_x$ films [80] and [$La(hfa)_3$·diglyme], [$Ba(hfa)_2$·tetraglyme] and $Cu(tmhd)_2$ used for the deposition of $La_{2-x}(Ba_x)CuO_{4-\delta}$ [70].

There is, therefore, unambiguous evidence that liquid "Ln$(hfa)_3$·glyme" adducts represent suitable solvents for other parent sources. These solutions are reliable multi-metal liquid single sources that, no doubt, are well suited for MOCVD applications.

5. Applications of "Ln$(hfa)_3$·L" sources to MOCVD depositions

The "Ln$(hfa)_3$·L" precursors have been widely adopted for the deposition of single component or complex oxide films. Their physico-chemical properties, in terms of thermal stability, volatility and mass-transport rate make them the best

source precursors to date known for conventional MOCVD of lanthanide phases and of several oxide systems, including CeO_2 [69,82–84], $LaAlO_3$ [27,79], $La_{2-x}(Ba_x)CuO_{4-\delta}$ [70], $YBa_2Cu_3O_{7-\delta}$ (YBaCuO) [58], and $YAlO_3$. Typical decomposition temperatures of these precursors are around 350 °C. These precursors can be safely used for deposition times of several hours. In particular in the case of CeO_2 growth from the $Ce(hfa)_3$·diglyme precursor deposition times up to 6 h have been adopted [84].

These precursors, however, might have some potential drawbacks due to the presence of F atoms in the molecular framework. Fluorine groups, in fact, while favoring both stabilities and vapor pressures might be incorporated in the growing films either as undesired contaminants or as fluoride phases. The use of H_2O-saturated O_2 stream as reaction gas in the MOCVD depositions, often proved capable of precluding fluorine contamination since the volatile HF can be easily desorbed from the growing films. In other cases, the competing (with oxide) fluoride phase is a volatile species that, similarly, can be pumped down in the exhaust [80].

In more general terms, the formation of competing fluoride phases is intimately associated with both thermodynamic stabilities and formation kinetics of potential growing phases. Thus, MOCVD of [$La(hfa)_3$·diglyme] single precursor forms the LaF_3 phase or, at higher O_2 flow, LaOF [55,56]. In the case of the parent homologous [$Pr(hfa)_3$·diglyme] precursor, the thermodynamic balance favors the growth of PrOF films over the PrO_{2-x} phases, even using H_2O saturated O_2 flow as reaction gas [68]. In the case of $LaAlO_3$ or YBaCuO films, the absence of fluoride side species is a clear indication that either $LaAlO_3$ or YBaCuO are thermodynamically more stable than the related LnF_3/LnOF or even of the BaF_2 phase. Another example of stabilization of a fluorine-free phase is related to the deposition of CeO_2 films. In this case, the adoption of the [$Ce(hfa)_3$·diglyme] as MOCVD cerium source produces pure CeO_2 films. CeF_3 does not form even when adopting dry oxygen as reaction gas, once deposition temperatures are used above the threshold temperature which thermodynamically favors the stabilization of the CeO_2 versus the CeF_3 phase. Therefore, the problem of unwanted fluorinated phases must be addressed from time to time, depending on the metal involved and, hence, on the thermodynamic stabilities of the desired phases.

Depositions of LnF_3/LnOF and CeO_2 films represent case studies of single-metal component films. The high volatility of the related metal precursors also allows deposition at atmospheric pressure. Thus, LaF_3 films can be deposited at atmospheric pressure from the [$La(hfa)_3$·diglyme] adduct [55]. Pure LaF_3 (Fig. 16) forms at lower temperatures (up to 600 °C). Upon increasing the temperature, in the 600–850 °C temperature range, the LaOF phase becomes more stable (Fig. 16). In both cases the metal precursor behaves as a multi-element source since it also supplies the fluorinating agent.

Similarly, (1 1 1) oriented PrF_3 films are deposited adopting the homologous [$Pr(hfa)_3$·diglyme] adduct and dry O_2 as reaction gas. The introduction of water vapor into the oxygen stream produces polycrystalline PrOF films with a (0 1 2) preferential texturing. A similar behaviour has been also found with the analogous Gd [52] and Eu [63] adducts. Systematic studies to preclude LnF_3/LnOF formation by varying the process parameters, including the deposition temperature and the water saturated oxygen partial pressure, proved unsuccessful.

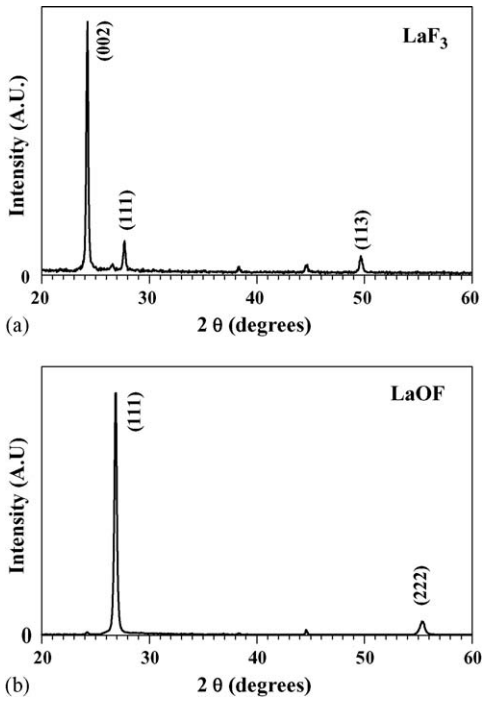

Fig. 16. XRD pattern of MOCVD grown LaF_3 and LaOF films deposited on (1 1 1) Si substrate using the $La(hfa)_3$·diglyme as a single source precursor.

Depositions made with the Ce homologue adduct produce high quality fluorine-free CeO_2 films on YSZ (100) substrate [2,83]. Thus, θ–2θ XRD pattern of these films, in addition to the YSZ (2 0 0) and (4 0 0) reflections, shows only the CeO_2 (2 0 0) and (4 0 0) reflections, thus pointing to a dominant ⟨1 0 0⟩ orientation of the polycrystalline films. The four poles at $\chi = 54.7°$ observed every 90° of φ in the (1 1 1) pole figure indicate a good in plane orientation.

Application of the multi-element sources mentioned above has also been expedient for the MOCVD deposition of $LaAlO_3$ and $YBa_2Cu_3O_{7-\delta}$ films.

The 1:1 La–Al molten source produces very homogeneous and smooth, mirror-like $LaAlO_3$ films over $SrTiO_3$ substrates [27,79]. Films as thick as 600 nm can be fabricated upon tuning the deposition time. A H_2O saturated O_2 flow is required as reaction gas to preclude fluorine contamination in the growing phase. Thus, the θ–2θ X-ray diffraction (XRD) pattern (Fig. 17a) shows, in addition to the (1 0 0) and (2 0 0) reflections expected for the $SrTiO_3$, two more features due to (1 0 0) and (2 0 0) reflections of the perovskite $LaAlO_3$ structure (indexing refers to the simple pseudo-cubic system). This is indication of a *c*-axis preferred orientation. The FWHM value of ≅0.4° measured in the rocking curve around the (2 0 0) $LaAlO_3$ reflection (Fig. 17b), indicates a good out-of-plane alignment of crystallites. Evidence of a good in-plane hetero-epitaxy is given by the four poles present in the (1 1 1) $LaAlO_3$ pole figure (Fig. 18). This, clearly, indicates a

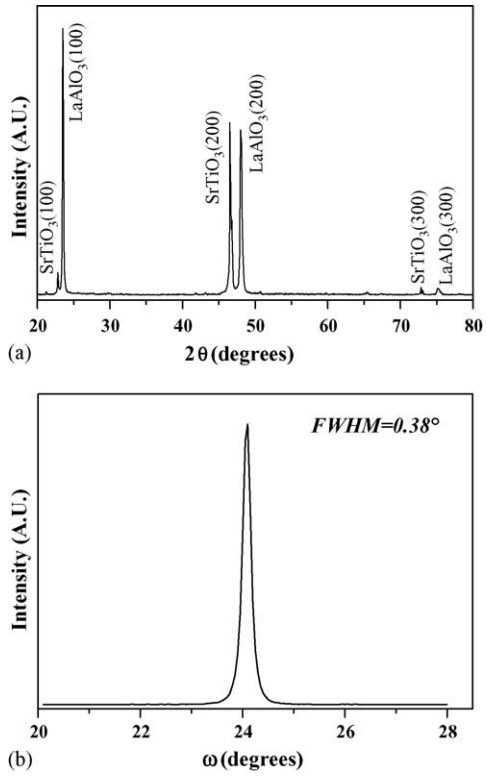

Fig. 17. XRD pattern (a) and the rocking curve of the $LaAlO_3$ (2 0 0) reflection (b) of an in situ deposited $LaAlO_3$ (1 0 0) film deposited on $SrTiO_3$ (1 0 0) at 1050 °C.

typical cube-on-cube growth:

$$[0\,0\,1]SrTiO_3||[0\,0\,1]LaAlO_3, \quad [1\,0\,0]SrTiO_3||[1\,0\,0]LaAlO_3$$

SEM images show high quality films with highly homogeneous surfaces consisting of ∼50–80 nm plate-like grains uniformly distributed (Fig. 19a). Atomic force microscopy (AFM) tapping mode measurements have indicated a root-mean-square (RMS) surface roughness of about 11 nm (Fig. 19b).

Moreover, energy dispersive X-Ray (EDX) analyses (Fig. 20) show that films have the expected 1:1 stoichiometry, not depending upon the substrate temperature in the entire (900–1050 °C) range. There is no evidence of fluorine incorporation. Films also possess good vertical homogeneity. Thus, X-ray photoelectron spectroscopy (XPS) depth profiles show that the La:Al:O 1:1:3 atomic ratio remain almost constant along the vertical section as expected for the $LaAlO_3$ phase. No C contamination is evident and F content is lower than 0.2%.

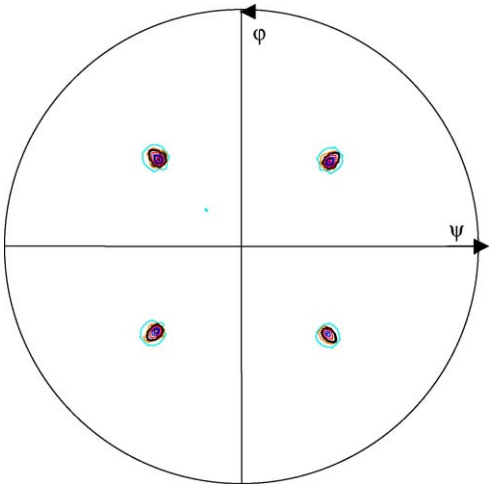

Fig. 18. (1 1 1) $LaAlO_3$ pole figure ($2\theta = 41.16°$).

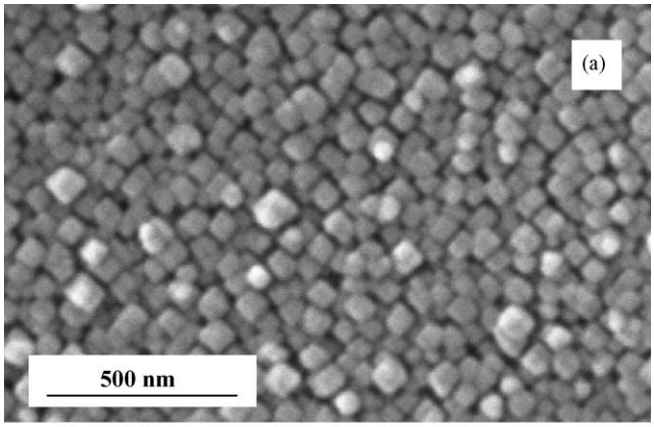

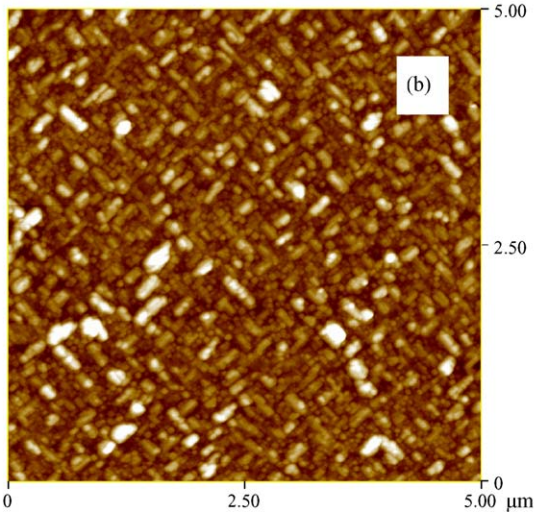

Fig. 19. SEM (a) and AFM (b) images of an in situ deposited $LaAlO_3$ (1 0 0) film on $SrTiO_3$ (1 0 0).

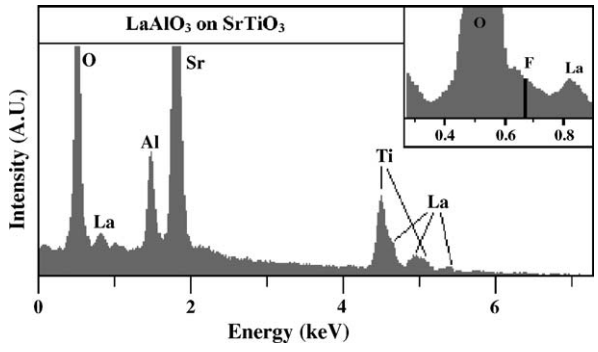

Fig. 20. EDX spectrum of an in situ deposited $LaAlO_3$ film on the $SrTiO_3$ substrate. The black line in the inset indicates the position of F Kα peak.

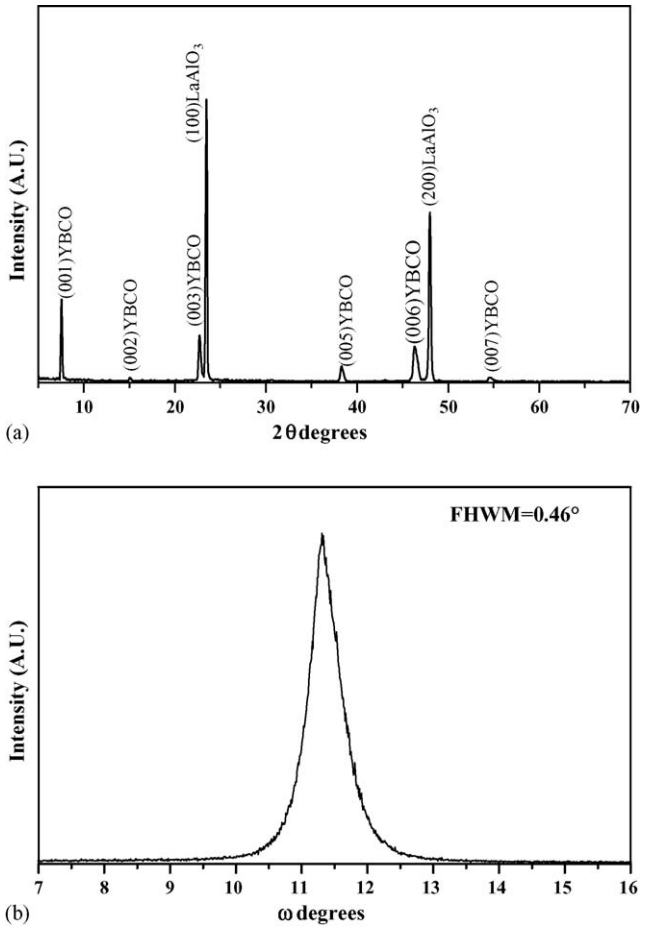

Fig. 21. X-ray diffraction pattern (a) and the rocking curve of the YBCO (0 0 3) reflection (b) of an MOCVD grown YBCO film on $LaAlO_3$ (1 0 0) substrate.

Similarly efficient growths of high T_c superconducting $YBa_2Cu_3O_{7-\delta}$ films on $LaAlO_3$ (1 0 0) substrates have been obtained using the multi-metal single source that uses the [Y(hfa)$_3$·monoglyme] precursor to dissolve the Ba and Cu precursors [58]. In particular, the mixture of the low-melting [Y(hfa)$_3$·monoglyme] and of [Ba(hfa)$_2$·tetraglyme] and Cu(tmhd)$_2$ sources has been used in the 1:2:0.5 Y:Ba:Cu ratio to yield YBaCuO films with the desired 1:2:3 stoichiometry at a deposition temperature of 800 °C. Of course, great attention has been paid to maintain the optimum oxygen partial pressure during the cooling–annealing process, because of its influence on phase transition from the insulating tetragonal to the superconducting orthorhombic phase. The X-ray diffraction pattern (Fig. 21a) shows all the (0 0 ℓ) peaks, thus indicating strongly *c*-axis aligned films. The small FWHM value (0.46°) of the (0 0 3) rocking curve (Fig. 21b) indicates an high degree of texturing. The intense four poles at $\Psi = 46°$ observed every 90° of φ in the (1 0 3) pole figure, indicate a good in-plane orientation of YBCO films on $LaAlO_3$ (1 0 0) substrate. Films always show smooth surfaces with "plate like" grains. Measurements of electrical transport properties give a critical temperature (T_c) value of 83 K and a critical current density (J_c) of 10^5 A/cm^2.

6. Conclusions

The present review highlights the most important issues regarding properties of rare-earth "second-generation" precursors and in particular relationships between the metal ionic radius and the coordination sphere and, ultimately, mass-transport properties and MOCVD capabilities. In fact, evidence has been found that the multidentate Lewis base glymes, adducted to metal β-diketonate fluorinated framework, prevent either oligomerization or water coordination, and, even more interesting, weaken lattice energies of crystals thus resulting in stable low melting, highly volatile molecules. Thus, we can choose a priori: (i) the coordination sphere that better fit the ionic radius of the particular rare-earth element, (ii) the best suited Lewis base, in terms of number of coordinating atoms, to preclude H_2O or solvent coordination for that specific ion and (iii) the coordination associated with the best properties in terms of thermal stability and volatility. Therefore, it is possible to tailor the architectural framework with the perspective of the best thermal properties and precursor volatilities.

To our knowledge the present "Ln(hfa)$_3$·glyme" complexes represent the best examples of thermally stable rare-earth β-diketonate polyether adducts. Their properties can be contrasted with those of the similar [La(tmhd)$_3$·tetraglyme] which decomposes upon sublimation to yield the unadducted tmhd complex. Even more interesting, thermogravimetric and vaporization rate experiments indicate that "second-generation" precursors can be used in atmospheric-pressure MOCVD deposition at temperatures lower than 200 °C with better mass-transport properties and thermal behaviour than conventional rare-earth metal CVD sources.

In addition, the rather low-melting points allow their use as thermally stable precursors in the liquid phase, hence under constant vaporization and mass-transport rates. Finally, the properties of the present precursors open intriguing possibilities for their use as liquid solvents for precursors of different metals, thus resulting in multi-metal, liquid single-sources for simultaneous delivering of stoichiometric mixture of different metals in simpler mono-component MOCVD reactor.

Their vapor-phase transport characteristics at low- and atmospheric-pressure make them attractive candidates not only for laboratory MOCVD processes but also for industrial applications.

References

[1] M.L. Hitchman, K.F. Jensen, Chemical Vapor Deposition: Principles and Applications, Academic Press, London, 1993.
[2] M. Razeghi, The MOCVD Challenge, vol. 1, Adam Hilger, Bristol, 1989.
[3] T. Kodas, M. Hampden-Smith, The Chemistry of Metal CVD, VCH, Weinheim, 1994.
[4] W.S. Rees, CVD of Non-Metals, VCH, Weinheim, 1996.
[5] T.J. Marks, Pure Appl. Chem. 67 (1995) 313.
[6] D.L. Schulz, T.J. Marks, Adv. Mater. 6 (1994) 719.
[7] M. Leskelä, H. Mölsä, L. Niinistö, Supercond. Sci. Technol. 6 (1993) 627, and references therein.

[8] R.C. Mehrotra, R. Bohra, D.P. Gaur, Metal β-Diketonates and Allied Derivatives, Academic Press, London, 1978.
[9] S.B. Turnipseed, R.M. Barkley, R.E. Sievers, Inorg. Chem. 30 (1991) 1164.
[10] A.P. Purdy, A.D. Berry, R.T. Holm, M. Fatemi, D.K. Gaskill, Inorg. Chem. 28 (1989) 2799.
[11] A.A. Drozdov, S.I. Trojanov, Polyhedron 11 (1992) 2877.
[12] G. Rossetto, A. Polo, F. Benetollo, M. Porchia, P. Zanella, Polyhedron 11 (1992) 979.
[13] J. Auld, A.C. Jones, A. Barry Leese, B. Cockayne, P.J. Wright, P. O'Brien, M. Motevalli, J. Mater. Chem. 3 (1993) 1203.
[14] D.C. Bradley, M. Hason, M.B. Hursthouse, M. Motevalli, O.F.Z. Khan, R.G. Pritchard, J.O. Williams, J. Chem. Soc. Chem. Commun. (1991) 575.
[15] F.A. Cotton, G. Wilkinson, C.A. Murillo, M. Bochmann, Advanced Inorganic Chemistry, 6th ed., Wiley/Interscience, 1999.
[16] M. Becht, T. Gerfin, K.-H. Dahmen, Chem. Mater. 5 (1993) 137.
[17] D. Chadwick, J. McAleese, K. Senkiw, B.C.H. Steele, Appl. Surf. Sci. 99 (1996) 417.
[18] S. Di Bella, A. Gulino, G. Lanza, I. Fragala, D. Stern, T.J. Marks, Organometallics 13 (1994) 3810.
[19] J.K. Marsh, J. Chem. Soc. (1947) 1084.
[20] K.N. Yang, Y. Dalichaouch, J.M. Ferreira, B.W. Lee, J.J. Neumeier, M.S. Torikachvili, H. Zhou, M.B. Maple, R.R. Hake, Solid State Commun. 63 (1987) 515.
[21] E.M. Engler, V.Y. Lee, A.I. Nazzal, R.B. Beyers, G. Lim, P.M. Grant, S.S.P. Parkin, M.L. Ramirez, J.E. Vasquez, R.J. Savoy, J. Am. Chem. Soc. 109 (1987) 2848.
[22] T. Rouillon, M. Hervieu, B. Domengès, B. Raveau, J. Solid State Chem. 103 (1993) 63.
[23] R.J. Cava, R.B. van Dover, B. Batlagg, E.A. Rietman, Phys. Rev. Lett. 58 (1987) 408.
[24] H. Müller-Buschbaum, Angew. Chem. Int. Ed. Engl. 28 (1989) 1472.
[25] X.F. Meng, F.S. Pierce, K.M. Wong, R.S. Amos, C.H. Xu, B.S. Deaver Jr., S.J. Poon, IEEE Trans. Magn. 27 (1991) 1638.
[26] A.A. Molodyk, A.R. Kaul, O.Yu. Gorbenko, M.A. Novojilov, I.E. Korsakov, G. Wahl, in: Proceedings of the 12th European Conference on Chemical Vapour Deposition, J. Phys. IV 2 (1999) 709.
[27] G. Malandrino, I.L. Fragalà, P. Scardi, Chem. Mater. 10 (1998) 3765.
[28] B. Han, D.A. Neumayer, D.L. Schulz, B.J. Hinds, T.J. Marks, Chem. Mater. 5 (1993) 14.
[29] C. Tian, Y. Du, S.-W. Chan, J. Vac. Sci. Technol. A 15 (1997) 85.
[30] H.J. Osten, J.P. Liu, H.J. Mussig, Appl. Phys. Lett. 80 (2002) 297.
[31] S.R. Drake, A. Lyons, D.J. Otway, A.M.Z. Slawin, D.J. Williams, J. Chem. Soc. Dalton Trans. (1993) 2379.
[32] G. Xu, Z.-M. Wang, Z. He, Z. Lü, C.-S. Liao, C.-H. Yan, Inorg. Chem. 41 (2002) 6802.
[33] K. Timmer, K.I.M.A. Spee, A. Mackor, H.A. Meinema, A.L. Spek, P. van der Sluis, Inorg. Chim. Acta 190 (1991) 109.
[34] K. Timmer, H.A. Meinema, Inorg. Chim. Acta 187 (1991) 99.
[35] P. van der Sluis, A.L. Spek, K. Timmer, H.A. Meinema, Acta Crystallogr. C 46 (1990) 1741.
[36] R. Gardiner, D.W. Brown, P.S. Kirlin, A.L. Rheingold, Chem. Mater. 3 (1991) 1053.
[37] S.R. Drake, S.A.S. Miller, D.J. Williams, Inorg. Chem. 32 (1993) 3227.
[38] J.A.T. Norman, G.P. Pez, J. Chem. Soc. Chem. Commun. (1991) 971.
[39] S.C. Thompson, D.J. Cole-Hamilton, D.D. Gilliland, M.L. Hitchman, J.C. Barnes, Adv. Mater. Opt. Electron. 1 (1992) 81.
[40] G. Malandrino, F. Castelli, I.L. Fragalà, Inorg. Chim. Acta 224 (1994) 203.
[41] G. Malandrino, I.L. Fragalà, D.A. Neumayer, C.L. Stern, B.J. Hinds, T.J. Marks, J. Mater. Chem. 4 (1994) 1061.
[42] D.A. Neumayer, D.B. Studebaker, B.J. Hinds, C.L. Stern, T.J. Marks, Chem. Mater. 6 (1994) 878.
[43] J.A.P. Nash, J.C. Barnes, D.J. Cole-Hamilton, B.C. Richards, S.L. Cook, M.L. Hitchman, Adv. Mater. Opt. Electron. 5 (1995) 1.
[44] J.A. Belot, D.A. Neumayer, C.J. Reedy, D.B. Studebaker, B.J. Hinds, C.L. Stern, T.J. Marks, Chem. Mater. 9 (1997) 1638.
[45] G. Malandrino, D.S. Richeson, T.J. Marks, D.C. DeGroot, J.L. Schindler, C.R. Kannewurf, Appl. Phys. Lett. 58 (1991) 182.
[46] M. Motevalli, P. O'Brein, I.M. Watson, Polyhedron 15 (1996) 1865.
[47] T.J. Marks, J.A. Belot, C.J. Reedy, R.J. McNeely, D.B. Studebaker, D.A. Neumayer, C.L. Stern, J. Alloys Comp. 251 (1997) 243C.
[48] S.R. Drake, M.B. Hursthouse, K.M.A. Malik, S.A.S. Miller, D.J. Otway, Inorg. Chem. 32 (1993) 4464.
[49] D.C. Bradley, H. Chudzynska, M.B. Hursthouse, M. Motevalli, Polyhedron 13 (1994) 7.
[50] I. Baxter, S.R. Drake, M.B. Hursthouse, K.M. Abdul Malik, J. MaAleese, D.J. Otway, J.C. Plakatouras, Inorg. Chem. 34 (1995) 1384.
[51] G. Malandrino, R. Licata, F. Castelli, I.L. Fragalà, C. Benelli, Inorg. Chem. 34 (1995) 6223.
[52] G. Malandrino, O. Incontro, F. Castelli, I.L. Fragalà, C. Benelli, Chem. Mater. 8 (1996) 1292.
[53] S.J. Kang, Y.S. Jung, Y.S. Sohn, Bull. Kor. Chem. Soc. 18 (1997) 75.
[54] S.J. Kang, Y.S. Jung, Y.S. Sohn, Bull. Kor. Chem. Soc. 18 (1997) 266.
[55] G. Malandrino, C. Benelli, F. Castelli, I.L. Fragalà, Chem. Mater. 10 (1998) 3434.
[56] G. Malandrino, I.L. Fragalà, S. Aime, W. Dastrù, R. Gobetto, C. Benelli, J. Chem. Soc. Dalton Trans. (1998) 1509.
[57] K.D. Pollard, J.J. Vittal, G.P.A. Yap, R.J. Puddephatt, J. Chem. Soc. Dalton Trans. (1998) 1265.
[58] G. Malandrino, R. Lo Nigro, I.L. Fragalà, C. Benelli, Eur. J. Inorg. Chem. (2004) 500.
[59] J.H. Lee, Y.S. Jung, Y.S. Sohn, S.J. Kang, Bull. Kor. Chem. Soc. 19 (1998) 231.
[60] S.J. Kang, Y.S. Jung, I.I.-H. Suh, Bull. Kor. Chem. Soc. 20 (1999) 95.
[61] K.D. Pollard, H.A. Jenkins, R.J. Puddephatt, Chem. Mater. 12 (2000) 701.
[62] G. Malandrino, R. Lo Nigro, F. Castelli, I.L. Fragalà, C. Benelli, Chem. Vap. Depos. 6 (2000) 233.
[63] G. Malandrino, M. Bettinelli, A. Speghini, I.L. Fragalà, Eur. J. Inorg. Chem. (2001) 1039.
[64] W.J. Evans, D.G. Giarikos, M.A. Johnston, M.A. Greci, W. Joseph, J. Chem. Soc. Dalton Trans. 4 (2002) 520.
[65] S.J. Kang, S.K. Lee, Bull. Kor. Chem. Soc. 24 (2003) 535.
[66] S.J. Kang, Bull. Kor. Chem. Soc. 25 (2004) 1207.
[67] J. Plakatouras, C. Kavounis, C. Cardin, Acta Cryst. E 59 (2003) m838.
[68] R. Lo Nigro, R.G. Toro, G. Malandrino, I.L. Fragalà, P. Rossi, P. Dapporto, J. Electrochem. Soc. 151 (2004) F-206.
[69] R. Lo Nigro, G. Malandrino, I.L. Fragalà, Chem. Mater. 13 (2001) 4402.
[70] G. Malandrino, L.M.S. Perdicaro, G.G. Condorelli, I.L. Fragalà, A. Cassinese, M. Barra, J. Mater. Chem. 15 (2005) 4718.
[71] R. Lo Nigro, G. Malandrino, I.L. Fragalà, M. Bettinelli, A. Speghini, J. Mater. Chem. 12 (2002) 2816.
[72] J.A. Belot, A. Wang, R.J. McNeely, L. Liable-Sands, A.L. Rheingold, T.J. Marks, Chem. Vap. Depos. 5 (1999) 65.
[73] L.N. Edleman, A. Wang, J.A. Belot, A.W. Metz, J.R. Babcock, A.M. Kawaoka, J. Ni, M.V. Metz, C.J. Flaschenriem, C.L. Stern, L.M. Liable-Sands, A.L. Rheingold, P.R. Markworth, R.P.H. Chang, M.P. Chudzik, C.R. Kannewurf, T.J. Marks, Inorg. Chem. 41 (2002) 5005.
[74] B.S. Lim, A. Rathu, J.-S. Park, R.G. Gordon, Inorg. Chem. 42 (2003) 7951.
[75] L. Armelao, D. Barreca, G. Bottaro, A. Gasparotto, C. Maragno, E. Tondello, Chem. Mater. 17 (2005) 427.
[76] J.A. Darr, D.M. Mingos, D.E. Hibbs, M.B. Hursthouse, K.M. Abdul Malik, Polyhedron 15 (1996) 3225.
[77] A. Gleizes, S. Sans-Lenain, D. Medus, N. Hovnanian, P. Miele, J.-D. Foulon, Inorg. Chim. Acta 209 (1993) 47.
[78] H.A. Luten, W.S. Rees Jr., V.L. Goedken, Chem. Vap. Depos. 2 (1996) 149.

[79] G. Malandrino, G.G. Condorelli, R. Lo Nigro, Chem. Vap. Depos. 10 (2004) 171.
[80] G. Malandrino, A.M. Borzì, I.L. Fragalà, A. Androne, A. Cassinese, G. Pica, J. Mater. Chem. 12 (2002) 3728.
[81] M.L. Hitchman, S.H. Shamlian, D.C. Gilliland, D. Cole-Hamilton, J.A.P. Nash, S.C. Thompson, S.L. Cook, J. Mater. Chem. 5 (1995) 47.
[82] R. Lo Nigro, R. Toro, G. Malandrino, I.L. Fragalà, Chem. Mater. 15 (2003) 1434.
[83] R. Lo Nigro, G. Malandrino, I.L. Fragalà, Mater. Sci. Eng. B 102 (2003) 323.
[84] R. Lo Nigro, R.G. Toro, G. Malandrino, I.L. Fragalà, J. Mater. Chem. 15 (2005) 2328.